

## Electronic Supplementary Information (ESI)

### **Rational design of 2D Janus $P3m1$ $M_2N_3$ (M=Cu, Zr, and Hf) and their surface-functionalized derivatives: ferromagnetic, piezoelectric, and photocatalytic properties†**

Heng Zhang,<sup>#a,b,c</sup> Frédéric Guégan,<sup>#c</sup> Junjie Wang,<sup>\*a</sup> Gilles Frapper<sup>\*c</sup>

<sup>a</sup>State Key Laboratory of Solidification Processing, School of Materials Science and Engineering, Northwestern Polytechnical University, Xi'an, Shaanxi 710072, People's Republic of China

<sup>b</sup>Institute of Semiconductors, Henan Academy of Sciences, Zhengzhou, Henan 450000, People's Republic of China

<sup>c</sup>Applied Quantum Chemistry group, E4, IC2MP, UMR 7285 Poitiers University-CNRS, 4 rue Michel Brunet TSA 51106 - 86073 Poitiers Cedex 9, France

†Electronic Supplementary Information (ESI) available: Methodological details; phonon dispersion curves; calculated elastic constants; AIMD simulations; crystallographic parameters; Manz bond orders, spin charge density; magnetic spin configurations; structures and DOS, piezoelectric coefficients (PDF)

<sup>#</sup>These authors contributed equally.

<sup>\*</sup>Correspondence and requests for materials should be addressed to Junjie Wang (wang.junjie@nwpu.edu.cn), Gilles Frapper (gilles.frapper@univ-poitiers.fr)

# CONSTENT

<b>S1 Methodology</b> .....	4
<b>S1.1 DFT calculations (VASP)</b> .....	4
<b>S1.2 Phonon dispersion calculations</b> .....	4
<b>S1.3 Mechanical properties</b> .....	4
<b>S1.4 <i>Ab initio</i> molecular dynamics simulations</b> .....	5
<b>S1.5 Carrier mobility</b> .....	5
<b>S1.6 Piezoelectric property calculations</b> .....	6
<b>S2. Results</b> .....	8
Fig. S1 Calculated phonon dispersion curves of 2D <i>P3m1</i> $M_2N_3$ by spin polarized GGA-PBE functional: (a) $Sc_2N_3$ , (b) $Ti_2N_3$ , (c) $V_2N_3$ , (d) $Cr_2N_3$ , (e) $Mn_2N_3$ , (f) $Fe_2N_3$ , (g) $Co_2N_3$ , (h) $Ni_2N_3$ , and (i) $Cu_2N_3$ .....	8
Fig. S2 Calculated phonon dispersion curves of 2D <i>P3m1</i> $M_2N_3$ by spin polarized GGA-PBE functional: (a) $Zn_2N_3$ , (b) $Y_2N_3$ , (c) $Zr_2N_3$ , (d) $Nb_2N_3$ , (e) $Mo_2N_3$ , (f) $Tc_2N_3$ , (g) $Ru_2N_3$ , (h) $Rh_2N_3$ , and (i) $Pd_2N_3$ .....	9
Fig. S3 Calculated phonon dispersion curves of 2D <i>P3m1</i> $M_2N_3$ by spin polarized GGA-PBE functional: (a) $Ag_2N_3$ , (b) $Cd_2N_3$ , (c) $Hf_2N_3$ , (d) $Ta_2N_3$ , (e) $W_2N_3$ , (f) $Re_2N_3$ , (g) $Os_2N_3$ , (h) $Ir_2N_3$ , and (i) $Pt_2N_3$ .....	10
Fig. S4 Calculated phonon dispersion curves of 2D <i>P3m1</i> $M_2N_3$ by spin polarized GGA-PBE functional: (a) $Au_2N_3$ , and (b) $Ag_2N_3$ .....	11
Table S1 Calculated elastic constants of 2D <i>P3m1</i> $M_2N_3$ (M=Co, Cu, Zr, and Hf) by GGA-PBE functional.....	11
Fig. S5 Energy fluctuations of 2D <i>P3m1</i> $M_2N_3$ during the AIMD simulations at specific temperatures, T = 300 and 600 K: (a) $Cu_2N_3$ , (b) $Zr_2N_3$ , and (c) $Hf_2N_3$ .....	12
Fig. S6 Radial distribution functions $g(r)$ of the Cu-Cu and Cu-N separations observed during AIMD simulations at T = 0, 300, and 600 K in the 2D <i>P3m1</i> $Cu_2N_3$ .....	13
Fig. S7 Radial distribution functions $g(r)$ of the Zr-Zr and Zr-N separations observed during AIMD simulations at T = 0, 300, and 600 K in the 2D <i>P3m1</i> $Zr_2N_3$ .....	13
Fig. S8 Radial distribution functions $g(r)$ of the Hf-Hf and Hf-N separations observed during AIMD simulations at T = 0, 300, and 600 K in the 2D <i>P3m1</i> $Hf_2N_3$ .....	14
Fig. S9 Snapshots of 2D <i>P3m1</i> $M_2N_3$ supercell (5×5) at ambient pressure at the end of 8 ps: (a) $Cu_2N_3$ , (b) $Zr_2N_3$ , and (c) $Hf_2N_3$ . The silver, blue, yellow, and green balls indicate the N, Cu, Zr, and Hf atoms, respectively. ....	14

Table S2 Calculated Manz bond orders of different N-M bonds of 2D $P3m1$ $M_2N_3$ (M= Cu, Zr, and Hf) by the GGA-PBE functional.....	15
Table S3 Crystallographic parameters of 2D $P3m1$ $M_2N_3$ (M=Cu, Hf, and Zr) by the spin-polarized GGA-PBE functional.....	15
Fig. S10 2D ELF contours of 2D $P3m1$ $M_2N_3$ (M= Cu, Zr, and Hf) by the GGA-PBE functional: (a) $Cu_2N_3$ , (b) $Zr_2N_3$ , and (c) $Hf_2N_3$ .....	16
Fig. S11 Possible anti-ferromagnetic (AFM) spin configurations of 2D $P3m1$ $M_2N_3$ (M=Cu, Zr, and Hf). In AFM-1~11, different spin states of $N^{td}$ and $N^{in}$ atoms are considered. In AFM-12~22, different spin states of $M^1$ atoms are considered. ....	16
Table S4 Calculated energies of ferromagnetic (FM), anti-ferromagnetic (AFM) and nonmagnetic (NM) spin configurations of $2 \times 2 \times 1$ supercells of 2D $P3m1$ $M_2N_3$ (M=Cu, Hf, and Zr) by spin-polarized GGA-PBE functional. After structure optimization, the AFM 10, 11, 21, 22 transformed into the FM states. ....	17
Table S5 Calculated energies of ferromagnetic, anti-ferromagnetic and nonmagnetic spin configurations of 2D $P3m1$ $M_2N_3$ (M=Cu, Hf, and Zr) by the spin-polarized HSE06 functional.....	17
Fig. S12 Spin charge density of 2D Janus $P3m1$ $M_2N_3$ : (a) $Cu_2N_3$ , (b) $Zr_2N_3$ , and (c) $Hf_2N_3$ . The red, yellow, and green balls indicate the Cu, Zr, and Hf atoms, respectively. In (a-c), the light blue and yellow contours indicate the spin-up and spin-down states, respectively. ....	18
Fig. S13 Six possible adsorption sites on the two facets of 2D $P3m1$ $M_2N_3$ (M=Cu, Zr, and Hf). The triangle, circle, and square (hexagon, oval, and pentagon) indicate the adsorption site of top (bottom) facet. The triangle sits above the $N^{in}$ site and the circle sits above the $N^{td}$ site, and the square sits above the $M^1$ site. The hexagon sits below the $M^2$ site, and the oval sits below the $M^1$ site, and the pentagon sits below the $N^{oh}$ site.....	18
Table S7 Formal charge of 2D $P3m1$ $3 \times 3 \times 1$ $M_2N_3$ and $M_2N_3-X$ (one ligand X (X=H, F, and Cl) absorbed $M_2N_3$ ) by Bader charge analysis. For the case of $M_2N_3-X$ , the $N^{td}$ indicates the N atoms bonded to X ligands.....	18
Fig. S14 Calculated phonon dispersion curves of 2D $P3m1$ $M_2N_3X$ (M=Cu, Hf, and Zr; X=H, F and Cl) by the GGA-PBE functional: (a) $Cu_2N_3H$ , (b) $Cu_2N_3F$ , (c) $Cu_2N_3Cl$ , (d) $Hf_2N_3H$ , (e) $Hf_2N_3F$ , (f) $Hf_2N_3Cl$ , (g) $Zr_2N_3H$ , (h) $Zr_2N_3F$ , and (i) $Zr_2N_3Cl$ .....	19
Fig. S15 Calculated phonon dispersion curves of 2D $P3m1$ $M_2N_3X_2$ (M=Cu, Zr, and Hf; X=H, F, and Cl) by GGA-PBE functional: (a) $Cu_2N_3H_2$ , (b) $Cu_2N_3F_2$ , (c) $Cu_2N_3Cl_2$ , (d) $Zr_2N_3H_2$ , (e) $Zr_2N_3F_2$ , (f) $Zr_2N_3Cl_2$ , (g) $Hf_2N_3H_2$ , (h) $Hf_2N_3F_2$ , and (i) $Hf_2N_3Cl_2$ .....	20
Table S8 Calculated crystallographic parameters of 2D $P3m1$ $Cu_2N_3H$ , $Cu_2N_3F$ , $Cu_2N_3Cl$ , $Zr_2N_3H$ , $Hf_2N_3H$ , and $Hf_2N_3F$ by the GGA-PBE functional.....	20
Fig. S16 Spin charge density of 2D $P3m1$ $Cu_2N_3X$ (X=H, F and Cl). The pink, silver and red balls are for X, N and Cu atoms, respectively. ....	22

Fig. S17 Rectangular lattices of 2D  $P3m1$   $Zr_2N_3H$ ,  $Hf_2N_3H$ , and  $Hf_2N_3F$ . The silver, yellow and pink balls are for N, M (Zr, Hf), and X (H, F) atoms, respectively. The equivalent lattice parameters  $a$ ,  $b$  of this rectangular cell are defined as  $x_0$  and  $y_0$ , respectively.....22

Fig. S18 Piezoelectric coefficients  $d_{11}$  (a, c) and  $d_{31}$  (b, d) of 2D  $P3m1$   $Zr_2N_3H$ ,  $Hf_2N_3H$ , and  $Hf_2N_3F$  via stacking effect. The mono, bi, and tri indicates the monolayer, trilayer, and trilayer of 2D  $P3m1$   $Zr_2N_3H$ ,  $Hf_2N_3H$ , and  $Hf_2N_3F$ , respectively.....23

**S3. Reference**.....24

## S1 Methodology

### S1.1 DFT calculations (VASP)

**Structural optimization.** First-principles calculations are performed using the projected-augmented-wave (PAW) method as implemented in VASP (version 5.4.4)<sup>1</sup>. Exchange-correlation energy is treated using Perdew-Burke-Ernzerhof (PBE) within the generalized gradient approximation (GGA).<sup>3,4</sup> A kinetic cutoff energy of 600 eV is used for the wavefunction expansion with a Monkhorst-Pack k mesh grid with a spacing of  $2\pi \times 0.04 \text{ \AA}^{-1}$ . This ensures that enthalpy converges to a criterion lower than  $1 \times 10^{-5}$  eV per cell, and forces to 0.01 eV/Å. The valence electron configurations considered in the calculation are H ( $1s^1$ ), N ( $2s^2 2p^3$ ), F ( $2s^2 2p^5$ ), Cl ( $3s^2 2p^5$ ), Cu ( $3d^{10} 4s^1$ ), Zr ( $4p^6 4d^2 5s^2$ ), and Hf ( $5p^6 5d^2 6s^2$ ).

**Energy band gap.** PBE functional has proven to be accurate for the description of structural properties of materials.<sup>13</sup> In contrast, it may underestimate the value of the band gaps. Therefore, we calculated the band gap at the Heyd-Scuseria-Ernzerhof (HSE06)<sup>5</sup> hybrid functional level of theory, using the optimized PBE structure (single-point energy calculation). This level of theory is noted thereafter as HSE06//PBE. During the band gap calculation, twenty k-points were used between two high-symmetric K-points in the reciprocal space ( $\Gamma$ -M-K- $\Gamma$ ), i.e.,  $\Gamma(0\ 0\ 0)$ ,  $M(0\ 1/2\ 0)$ , and  $K(-1/3\ 2/3\ 0)$ .

**Chemical bonding analysis.** To study the chemical bonding, electron localization function (ELF), Manz bond orders,<sup>6</sup> bader charge analysis,<sup>7</sup> and density of states (DOS) from the optimized geometries were also analyzed.

**Structural parameters analysis and images.** Finally, images of the crystalline structures were produced using VESTA software.<sup>8</sup>

### S1.2 Phonon dispersion calculations

In this work, first principles phonon calculations with density functional perturbation theory (DFPT) at a quasi-harmonic level were done using the open-source package PHONOPY (<https://phonopy.github.io/phonopy/>).<sup>9</sup> Supercells of 2D structures with displacements were created from a unit cell considering all possible crystal symmetry operations. In general, a  $3 \times 3$  supercell is sufficient, but larger ones can be required to avoid unphysical imaginary frequencies needed.

### S1.3 Mechanical properties

A necessary condition for the thermodynamic stability of a crystal lattice is that the crystal should be mechanically stable with respect to arbitrary (small) homogeneous deformations. Elastic stability criteria for bulk cubic crystals and more different crystal classes was well understood in the work of Born and co-authors.<sup>10, 11, 12</sup> The elastic tensor is determined by performing six finite distortions of the lattice and deriving the elastic constants from the strain-stress relationship.<sup>13</sup>

The elastic matrix of 2D materials was decreased into  $3 \times 3$  and six elastic constants are  $C_{11}$ ,  $C_{12}$ ,  $C_{22}$ ,  $C_{16}$ ,  $C_{26}$  and  $C_{66}$  using the standard Voigt notation:  $l$ -xx,  $2$ -yy,  $6$ -xy. In 2D rectangular unit-cells,  $C_{16}$  and  $C_{26}$  are zero. The calculated elastic constants  $C_{11}$ ,  $C_{12}$ ,  $C_{22}$  and  $C_{66}$  in 2D materials should satisfy necessary mechanical equilibrium conditions for mechanical stability:  $C_{11}C_{22}-C_{12}C_{21}>0$  and  $C_{11}, C_{22}, C_{66}>0$ .<sup>14, 15</sup>

In terms of these elastic constants, the 2D Young's moduli (in-plane stiffness) for the strain in the  $[10]$  and  $[01]$  direction are,<sup>16</sup>

$$Y_{21} = (C_{11}C_{22}-C_{12}C_{12})/C_{22}, \quad (\text{eq.1})$$

$$Y_{12} = (C_{11}C_{22}-C_{12}C_{12})/C_{11}. \quad (\text{eq.2})$$

#### S1.4 *Ab initio* molecular dynamics simulations

**Thermal stability.** *Ab initio* molecular dynamics (AIMD) simulations based on DFT PBE calculations were carried out using VASP code to examine the thermal stabilities of 2D  $P3m1$   $\text{Cu}_2\text{N}_3$ ,  $\text{Hf}_2\text{N}_3$ , and  $\text{Zr}_2\text{N}_3$  structures. AIMD calculations with NVT ensemble and Andersen thermostat were performed at 300 K and 600 K.<sup>17</sup> The timestep was 1 fs, and the total simulation time was as long as 8 ps. In such AIMD simulations,  $5 \times 5 \times 1$  supercells of 2D  $P3m1$   $\text{Cu}_2\text{N}_3$ ,  $\text{Hf}_2\text{N}_3$ , and  $\text{Zr}_2\text{N}_3$  phases were employed. The Brillouin zone integration was restricted to the  $\Gamma$  point of the supercell, due to a high calculation cost.

#### S1.5 Carrier mobility

The intrinsic carrier mobility  $m$  of 2D crystals was investigated within the framework of the deformation potential theory for semiconductors proposed by Bardeen and Shockley.<sup>24</sup> In the long-wavelength limit, when only the interaction between electron and longitudinal acoustic phonon is taken into consideration, the carrier mobility of 2D crystals can be expressed by following formula,<sup>18</sup>

$$\mu = \frac{eh^3 C_{2D}}{kT m_{e(h)}^* m_d^* E_l^2}, \quad (\text{eq.3})$$

in which  $e$  is electron charge,  $\hbar$  is the reduced Planck's constant,  $T$  is temperature (300K in this work),  $m_{e(h)}^*$  is effective mass of electron or hole determined by

$$m_{e(h)}^* = \frac{\hbar^2}{(\partial^2 E(k) / \partial k^2)}$$

$m_d^*$  is the average effective mass along  $x$  and  $y$  directions defined by  $(m_x^* m_y^*)^{1/2}$ .

The 2D elastic modulus  $C_{2D}$  of the longitudinal strain in the propagation directions ( $x$ ,  $y$ ) of the longitudinal acoustic wave was derived from  $(E - E_0) / S_0 = C_{2D} (\Delta l / l_0)^2 / 2$ , where  $E(E_0)$  is the total energy,  $S_0$  is the equilibrium lattice area of 2D crystals,  $\Delta l$  is the small dilation of the lattice constant  $l_0$  along the transport direction.  $E_l$  is the deformation potential constant, given by  $E_l^{e(h)} = \Delta E_{CBM(VBM)} / (\Delta l / l_0)$  in which  $\Delta E_{CBM(VBM)}$  is the energy shift of valance band maximum (VBM) and conduction band minimum (CBM) with respect to the vacuum level. Though PBE calculations always underestimate the band gap values in semiconductors, PBE functional can predict correct curvatures of valence and conduction bands and the calculated carrier mobilities using PBE are in good agreement with the experiments in numerous 2D crystals.<sup>19</sup>

## S1.6 Piezoelectric property calculations

In the non-centrosymmetric crystals, a change of polarization can be induced by strain or stress. The phenomenon can be described by the third-rank piezoelectric stress tensors  $e_{ijk}$  and strain tensor  $d_{ijk}$ , which are the sum of ionic and electronic components,<sup>20</sup>

$$e_{ijk} = \frac{\partial P_i}{\partial \varepsilon_{jk}} = e_{ijk}^{elec} + e_{ijk}^{ion}, \quad (\text{eq.4})$$

$$d_{ijk} = \frac{\partial P_i}{\partial \sigma_{jk}} = d_{ijk}^{elec} + d_{ijk}^{ion}, \quad (\text{eq.5})$$

in which,  $P_i$ ,  $e_{jk}$ , and  $d_{jk}$  are polarization vector, strain, and stress, correspondingly. The density functional perturbation theory (DFPT) has been used to calculate the relaxed ion-piezoelectric stress and coefficients, as incorporated into VASP code<sup>21</sup>.

In the present work of 2D materials, only in-plane strain components using Voigt notation are considered and the  $d_{ij}$  can be derived by the following formula,<sup>20</sup>

$$\begin{pmatrix} e_{11} & e_{12} & e_{13} \\ e_{21} & e_{22} & e_{23} \\ e_{31} & e_{32} & e_{33} \end{pmatrix} = \begin{pmatrix} d_{11} & d_{12} & d_{13} \\ d_{21} & d_{22} & d_{23} \\ d_{31} & d_{32} & d_{33} \end{pmatrix} \begin{pmatrix} C_{11} & C_{12} & C_{13} \\ C_{21} & C_{22} & C_{23} \\ C_{31} & C_{32} & C_{33} \end{pmatrix}. \quad (\text{eq.6})$$

Since 2D  $M_2N_3$  and their surface-functionalized derivatives crystallizes into the

space group  $P3m1$  (No. 156) with a  $3m$  point group symmetry, the (eq.6) can be further reduced below,<sup>[22]</sup>

$$\begin{pmatrix} e_{11} & -e_{11} & 0 \\ 0 & 0 & -e_{11}/2 \\ e_{31} & e_{31} & 0 \end{pmatrix} = \begin{pmatrix} d_{11} & -d_{11} & 0 \\ 0 & 0 & -2d_{21} \\ d_{31} & d_{31} & 0 \end{pmatrix} \begin{pmatrix} C_{11} & C_{12} & 0 \\ C_{12} & C_{22} & 0 \\ 0 & 0 & \frac{C_{11}+C_{12}}{2} \end{pmatrix} \quad (\text{eq.7})$$

According to equations (eq.7),  $d_{11}$  and  $d_{31}$  can be expressed as following,

$$d_{11} = \frac{e_{11}}{C_{11} - C_{12}}, \quad (\text{eq.8})$$

$$d_{31} = \frac{e_{31}}{C_{11} + C_{12}}. \quad (\text{eq.9})$$

## S2. Results

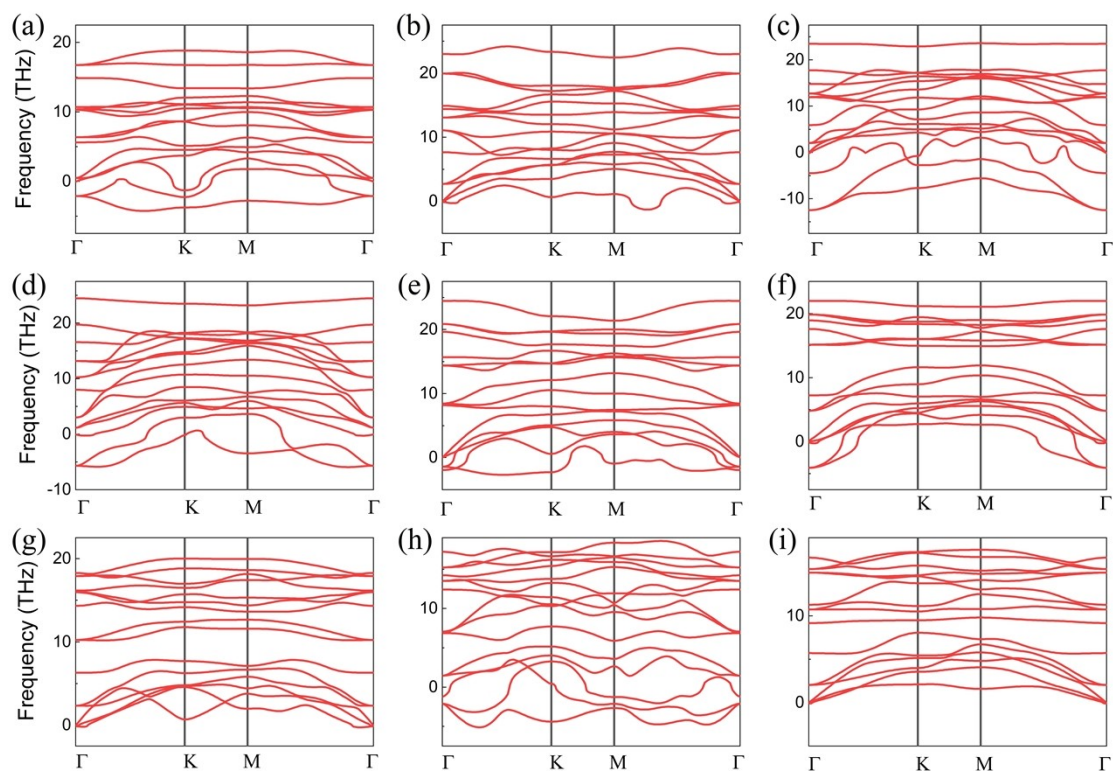


Fig. S1 Calculated phonon dispersion curves of 2D  $P3m1$   $M_2N_3$  by spin polarized GGA-PBE functional: (a)  $Sc_2N_3$ , (b)  $Ti_2N_3$ , (c)  $V_2N_3$ , (d)  $Cr_2N_3$ , (e)  $Mn_2N_3$ , (f)  $Fe_2N_3$ , (g)  $Co_2N_3$ , (h)  $Ni_2N_3$ , and (i)  $Cu_2N_3$

In Fig. S1, no imaginary phonon modes are found in the whole Brillouin zone of (g)  $Co_2N_3$  and (i)  $Cu_2N_3$ , which confirms their dynamical stabilities. The large imaginary frequencies indicates that (a)  $Sc_2N_3$ , (b)  $Ti_2N_3$ , (c)  $V_2N_3$ ; (d)  $Cr_2N_3$ , (e)  $Mn_2N_3$ , (f)  $Fe_2N_3$ , and (h)  $Ni_2N_3$  are dynamically unstable.

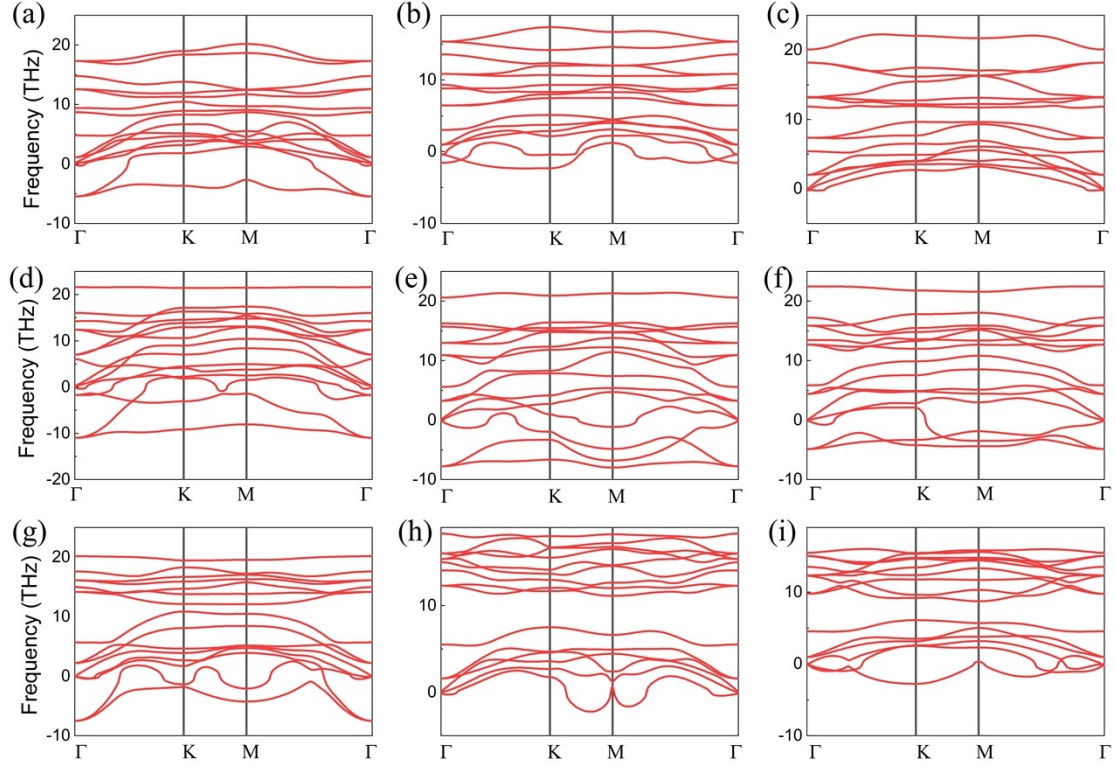


Fig. S2 Calculated phonon dispersion curves of 2D  $P3m1$   $M_2N_3$  by spin polarized GGA-PBE functional: (a)  $Zn_2N_3$ , (b)  $Y_2N_3$ , (c)  $Zr_2N_3$ , (d)  $Nb_2N_3$ , (e)  $Mo_2N_3$ , (f)  $Tc_2N_3$ , (g)  $Ru_2N_3$ , (h)  $Rh_2N_3$ , and (i)  $Pd_2N_3$

In Fig. S2, although a slight imaginary phonon mode close to  $\Gamma$  point is found for (c)  $Zr_2N_3$ , its dynamical stability is still confirmed because it is worth noting that this is a general phenomenon observed in 2D materials, including the well-studied graphene, hexagonal borophene, and  $CrI_3$ .<sup>23, 24</sup> The very small region of imaginary frequency (shown as negative) near the  $\Gamma$  point is an artifact from the Fourier interpolation, as discussed in reference 25. Whereas the large imaginary frequencies indicates that (a)  $Zn_2N_3$ , (b)  $Y_2N_3$ , (d)  $Nb_2N_3$ , (e)  $Mo_2N_3$ , (f)  $Tc_2N_3$ , (g)  $Ru_2N_3$ , (h)  $Rh_2N_3$ , and (i)  $Pd_2N_3$  are dynamically unstable.

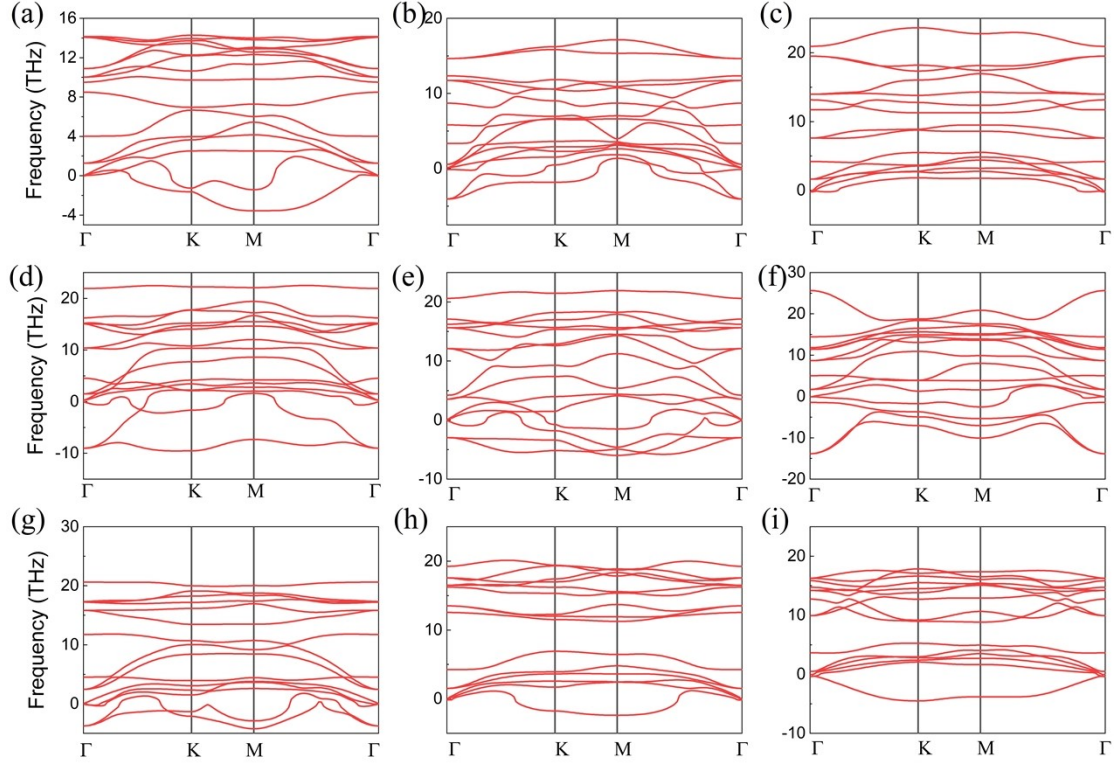


Fig. S3 Calculated phonon dispersion curves of 2D  $P3m1$   $M_2N_3$  by spin polarized GGA-PBE functional: (a)  $Ag_2N_3$ , (b)  $Cd_2N_3$ , (c)  $Hf_2N_3$ , (d)  $Ta_2N_3$ , (e)  $W_2N_3$ , (f)  $Re_2N_3$ , (g)  $Os_2N_3$ , (h)  $Ir_2N_3$ , and (i)  $Pt_2N_3$

In Fig. S3, a slight imaginary phonon mode close to  $\Gamma$  point is found for (c)  $Hf_2N_3$ , which confirms its dynamical stability. The very small region of imaginary frequency (shown as negative) near the  $\Gamma$  point is an artifact from the Fourier interpolation, as discussed in reference 25. Whereas the large imaginary frequencies indicates that (a)  $Ag_2N_3$ , (b)  $Cd_2N_3$ , (d)  $Ta_2N_3$ , (e)  $W_2N_3$ , (f)  $Re_2N_3$ , (g)  $Os_2N_3$ , (h)  $Ir_2N_3$ , and (i)  $Pt_2N_3$  are dynamically unstable.

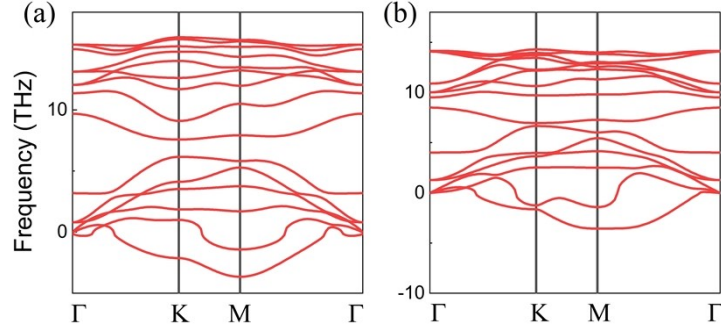


Fig. S4 Calculated phonon dispersion curves of 2D  $P3m1$   $M_2N_3$  by spin polarized GGA-PBE functional: (a)  $Au_2N_3$ , and (b)  $Ag_2N_3$

In Fig. S4, the large imaginary frequencies indicates that (a)  $Au_2N_3$  and (b)  $Ag_2N_3$  are dynamically unstable.

Table S1 Calculated elastic constants of 2D  $P3m1$   $M_2N_3$  (M=Co, Cu, Zr, and Hf) by GGA-PBE functional

Phase	$C_{11}$ (N/m)	$C_{12}$ (N/m)	$C_{22}$ (N/m)	$C_{33}$ (N/m)
$Co_2N_3$	49.28	190.99	49.28	-70.85
$Cu_2N_3$	57.43	15.05	57.43	21.19
$Zr_2N_3$	172.46	82.84	172.46	44.81
$Hf_2N_3$	180.92	93.67	180.92	43.63

Fig. S1-S4 show that 2D  $P3m1$   $M_2N_3$  (M=Co, Cu, Hf, and Zr) exhibit good dynamical stability, so the elastic constants of these four compounds were only presented here. Obviously, it is found that 2D  $P3m1$   $Co_2N_3$  does not satisfy necessary mechanical equilibrium conditions for mechanical stability:  $C_{11}C_{22}-C_{12}C_{21}>0$ , and  $C_{66}>0$ .

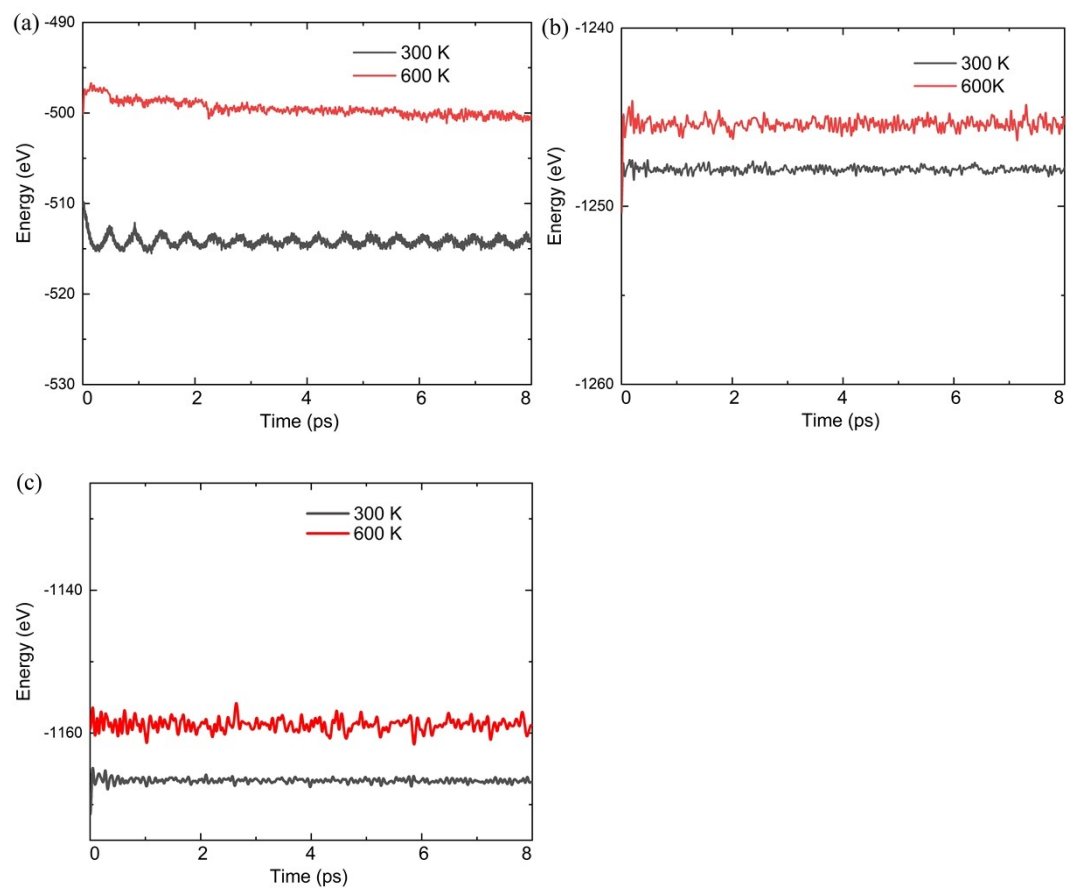


Fig. S5 Energy fluctuations of 2D  $P3m1$   $M_2N_3$  during the AIMD simulations at specific temperatures,  $T = 300$  and  $600$  K: (a)  $Cu_2N_3$ , (b)  $Zr_2N_3$ , and (c)  $Hf_2N_3$

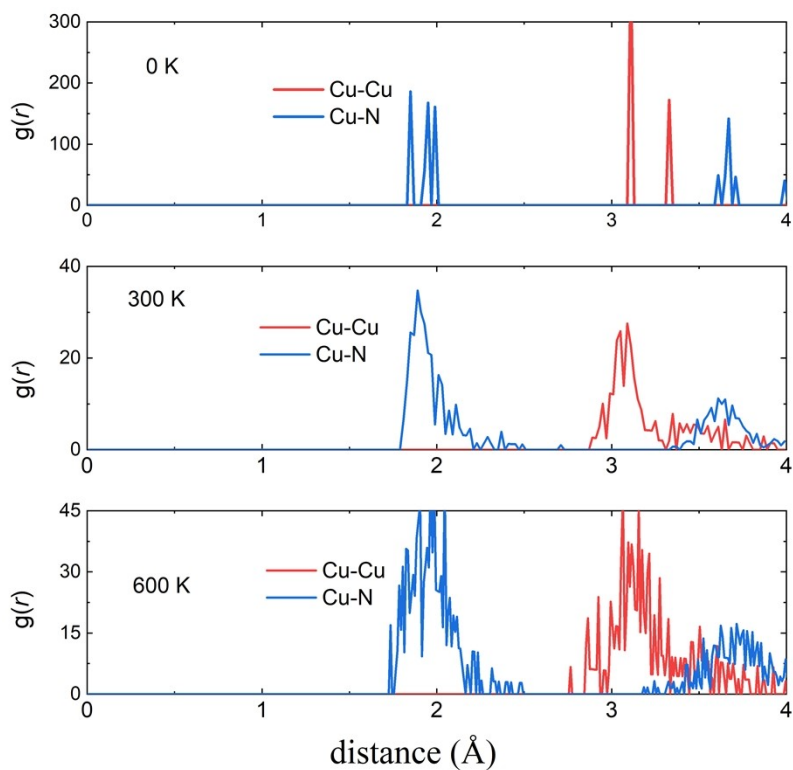


Fig. S6 Radial distribution functions  $g(r)$  of the Cu-Cu and Cu-N separations observed during AIMD simulations at  $T = 0, 300,$  and  $600$  K in the 2D  $P3m1$   $\text{Cu}_2\text{N}_3$

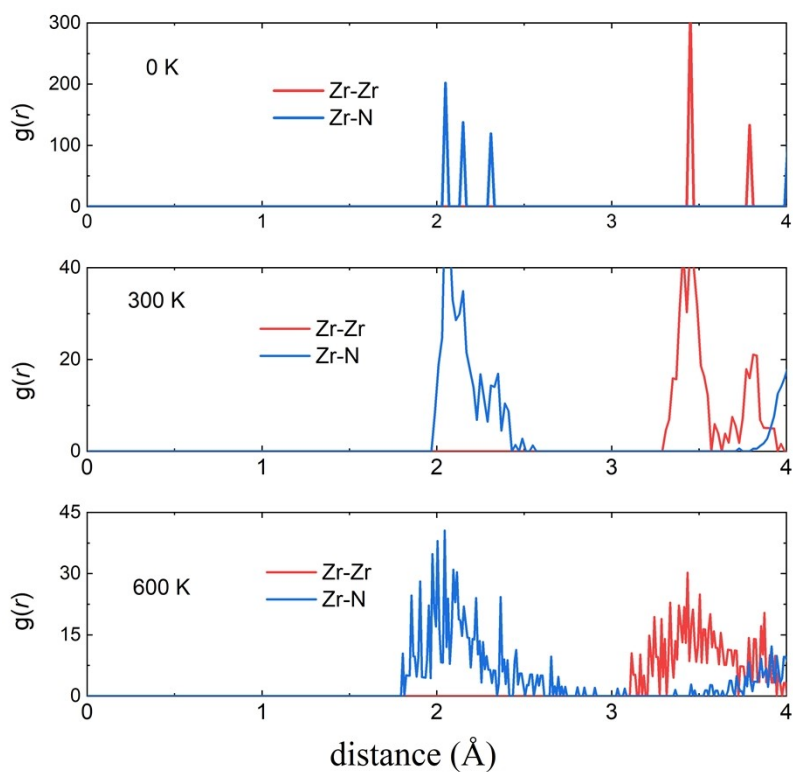


Fig. S7 Radial distribution functions  $g(r)$  of the Zr-Zr and Zr-N separations observed during AIMD simulations at  $T = 0, 300,$  and  $600$  K in the 2D  $P3m1$   $\text{Zr}_2\text{N}_3$

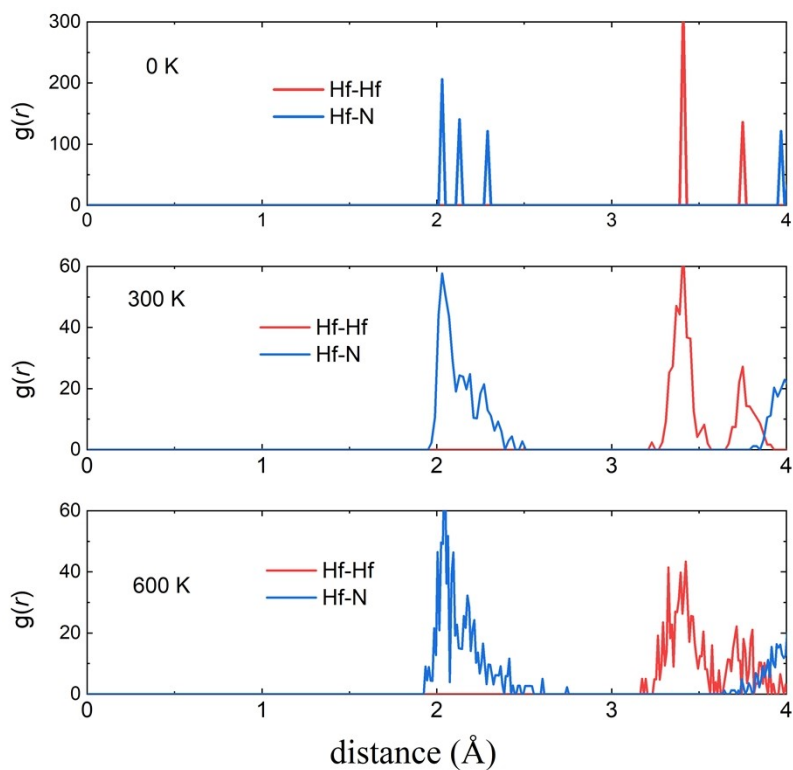


Fig. S8 Radial distribution functions  $g(r)$  of the Hf-Hf and Hf-N separations observed during AIMD simulations at  $T = 0, 300,$  and  $600$  K in the 2D  $P3m1$   $\text{Hf}_2\text{N}_3$

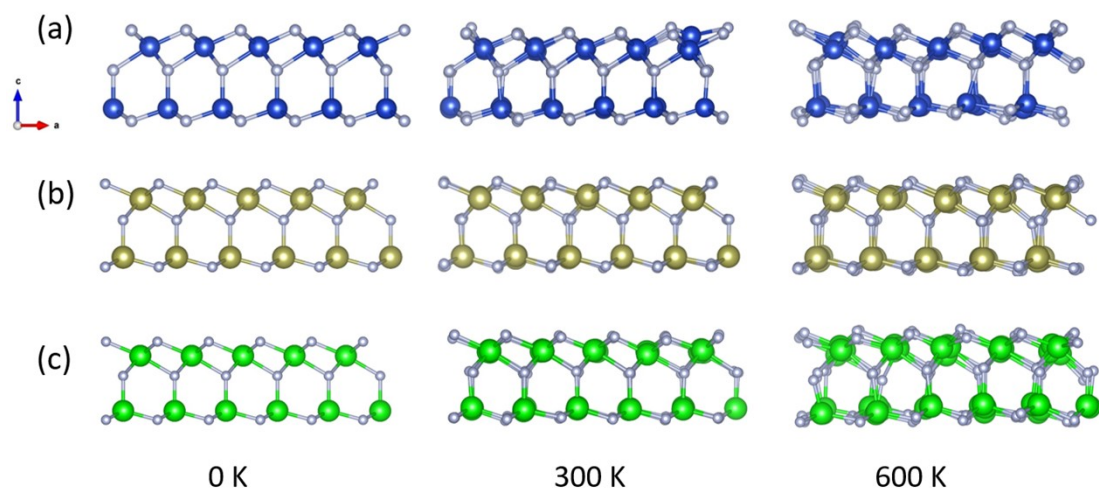


Fig. S9 Snapshots of 2D  $P3m1$   $\text{M}_2\text{N}_3$  supercell ( $5 \times 5$ ) at ambient pressure at the end of 8 ps: (a)  $\text{Cu}_2\text{N}_3$ , (b)  $\text{Zr}_2\text{N}_3$ , and (c)  $\text{Hf}_2\text{N}_3$ . The silver, blue, yellow, and green balls indicate the N, Cu, Zr, and Hf atoms, respectively.

Table S2 Calculated Manz bond orders of different N-M bonds of 2D  $P3m1$   $M_2N_3$  (M= Cu, Zr, and Hf) by the GGA-PBE functional

Phase	$N^{td}-X$		$N^{oh}-M$	
	bond distance	Manz bond order	bond distance	Manz bond order
$Cu_2N_3$	1.95 Å	0.48	1.84 Å	0.79
$Zr_2N_3$	2.15 Å	0.61	2.06 Å	0.85
$Hf_2N_3$	2.14 Å	0.66	2.04 Å	0.90

Table S3 Crystallographic parameters of 2D  $P3m1$   $M_2N_3$  (M=Cu, Hf, and Zr) by the spin-polarized GGA-PBE functional

Phase	Z	Space Group	Lattice parameters (Å,°)	Atomic coordinates (fractional)
$Cu_2N_3$	1	$P3m1$ SG 156	$a=b=3.11,$ $c=38.12,$ $\alpha=\beta=90.0, \gamma=120.0$	Cu 1c (0.67 0.33 0.17) Cu 1b (0.33 0.67 0.25) N 1b (0.33 0.67 0.20) N 1a (0.00 0.00 0.26) N 1a (0.00 0.00 0.15)
$Zr_2N_3$	1	$P3m1$ SG 156	$a=b=3.45,$ $c=30.96,$ $\alpha=\beta=90.0, \gamma=120.0$	Zr 1c (0.67 0.33 0.84) Zr 1a (0.00 0.00 0.74) N 1b (0.33 0.67 0.72) N 1b (0.33 0.67 0.87) N 1a (0.00 0.00 0.80)
$Hf_2N_3$	1	$P3m1$ SG 156	$a=b=3.41,$ $c=31.78,$ $\alpha=\beta=90.0, \gamma=120.0$	Hf 1c (0.67 0.33 0.16) Hf 1b (0.33 0.67 0.26) N 1b (0.33 0.67 0.20) N 1a (0.00 0.00 0.28) N 1a (0.00 0.00 0.13)

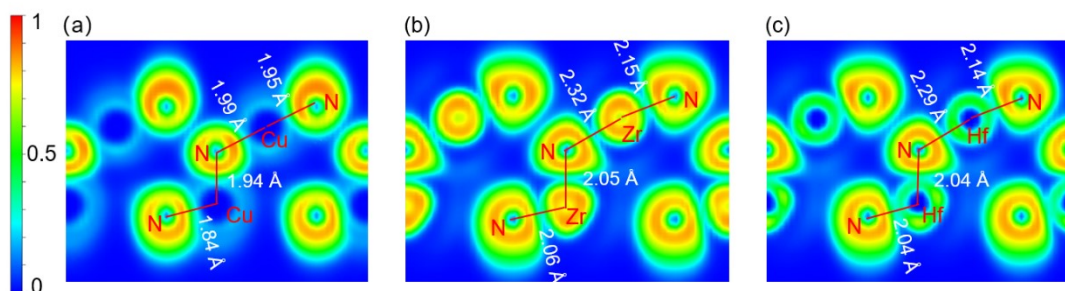


Fig. S10 2D ELF contours of 2D  $P3m1$   $M_2N_3$  ( $M=$  Cu, Zr, and Hf) by the GGA-PBE functional: (a)  $Cu_2N_3$ , (b)  $Zr_2N_3$ , and (c)  $Hf_2N_3$

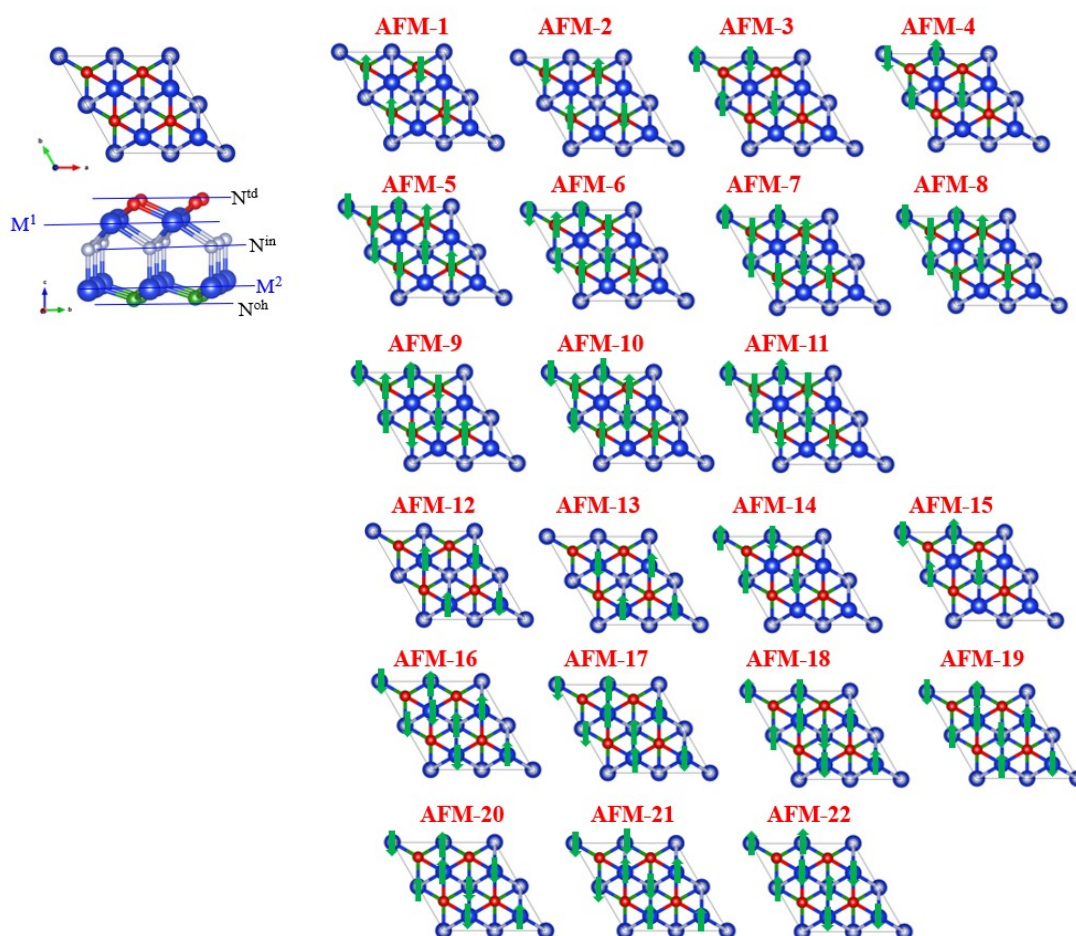


Fig. S11 Possible anti-ferromagnetic (AFM) spin configurations of 2D  $P3m1$   $M_2N_3$  ( $M=$  Cu, Zr, and Hf). In AFM-1~11, different spin states of  $N^{td}$  and  $N^{in}$  atoms are considered. In AFM-12~22, different spin states of  $M^1$  atoms are considered.

Table S4 Calculated energies of ferromagnetic (FM), anti-ferromagnetic (AFM) and nonmagnetic (NM) spin configurations of  $2 \times 2 \times 1$  supercells of 2D  $P3m1$   $M_2N_3$  (M=Cu, Hf, and Zr) by spin-polarized GGA-PBE functional. After structure optimization, the AFM 10, 11, 21, 22 transformed into the FM states.

Phase	Energy (eV)					
	AFM				FM	NM
	1~9	10~11	12~20	21~22		
$Cu_2N_3$	-98.69	-98.82	-98.69	-98.82	-98.82	-98.69
$Zr_2N_3$	-186.83	-187.06	-186.83	-187.06	-187.06	-186.83
$Hf_2N_3$	-200.01	-200.31	-200.01	-200.31	-200.31	-200.01

Table S5 Calculated energies of ferromagnetic, anti-ferromagnetic and nonmagnetic spin configurations of 2D  $P3m1$   $M_2N_3$  (M=Cu, Hf, and Zr) by the spin-polarized HSE06 functional

Phase	Energy (eV)					
	AFM				FM	NM
	1-9	10, 11	12-20	21, 22		
$Cu_2N_3$	-110.65	-112.32	-110.65	-112.32	-112.32	-110.65
$Hf_2N_3$	-234.33	-236.30	-234.33	-236.30	-236.30	-234.33
$Zr_2N_3$	-220.71	-222.46	-220.71	-222.46	-222.46	-220.71

Table S6 Average formal charges of M and N atoms in the 2D  $P3m1$   $M_2N_3$  by Bader charge analysis

	Formal charge ( e )	
	M	N
$Cu_2N_3$	+1.00	-0.67
$Hf_2N_3$	+2.23	-1.49
$Zr_2N_3$	+2.19	-1.46

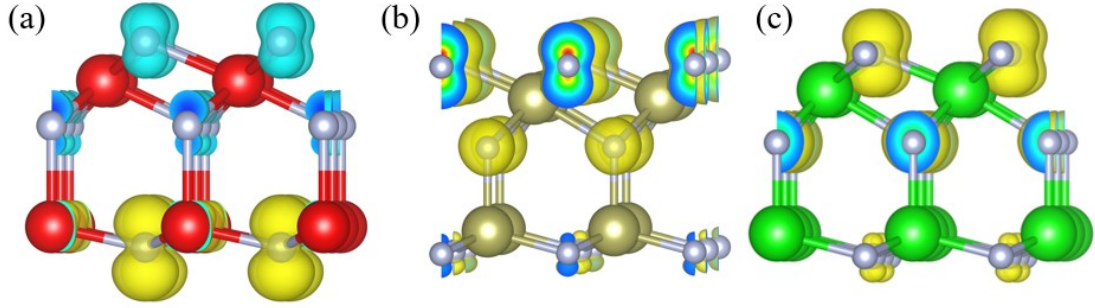


Fig. S12 Spin charge density of 2D Janus  $P3m1$   $M_2N_3$ : (a)  $Cu_2N_3$ , (b)  $Zr_2N_3$ , and (c)  $Hf_2N_3$ . The red, yellow, and green balls indicate the Cu, Zr, and Hf atoms, respectively. In (a-c), the light blue and yellow contours indicate the spin-up and spin-down states, respectively.

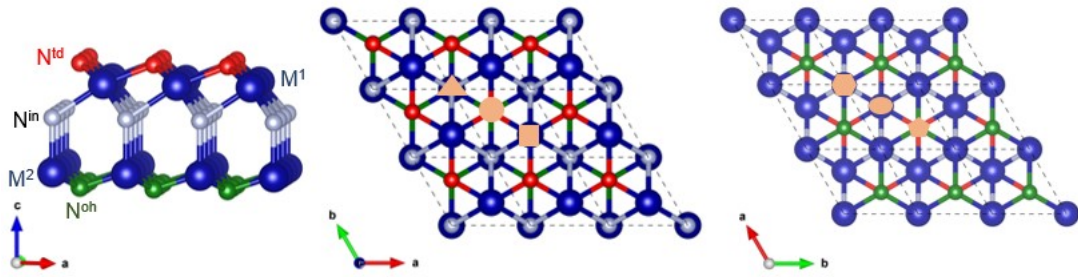


Fig. S13 Six possible adsorption sites on the two facets of 2D  $P3m1$   $M_2N_3$  ( $M=Cu, Zr,$  and  $Hf$ ). The triangle, circle, and square (hexagon, oval, and pentagon) indicate the adsorption site of top (bottom) facet. The triangle sits above the  $N^{in}$  site and the circle sits above the  $N^{td}$  site, and the square sits above the  $M^1$  site. The hexagon sits below the  $M^2$  site, and the oval sits below the  $M^1$  site, and the pentagon sits below the  $N^{oh}$  site.

Table S7 Formal charge of 2D  $P3m1$   $3 \times 3 \times 1$   $M_2N_3$  and  $M_2N_3-X$  (one ligand X ( $X=H, F,$  and  $Cl$ ) absorbed  $M_2N_3$ ) by Bader charge analysis. For the case of  $M_2N_3-X$ , the  $N^{td}$  indicates the N atoms bonded to X ligands.

	Formal charge ( $ e $ )	
	$N^{td}$	X
$Cu_2N_3$	-0.57	—
$Cu_2N_3-H$	-0.88	+0.42
$Cu_2N_3-F$	-0.77	-0.29
$Cu_2N_3-Cl$	-0.62	+0.17

$\text{Hf}_2\text{N}_3$	-1.31	—
$\text{Hf}_2\text{N}_3\text{-H}$	-1.53	+0.48
$\text{Hf}_2\text{N}_3\text{-F}$	-1.41	-0.28
$\text{Hf}_2\text{N}_3\text{-Cl}$	-1.33	0.08
$\text{Zr}_2\text{N}_3$	-1.32	—
$\text{Zr}_2\text{N}_3\text{-H}$	-1.58	+0.54
$\text{Zr}_2\text{N}_3\text{-F}$	-1.68	-0.36
$\text{Zr}_2\text{N}_3\text{-Cl}$	-1.36	+0.15

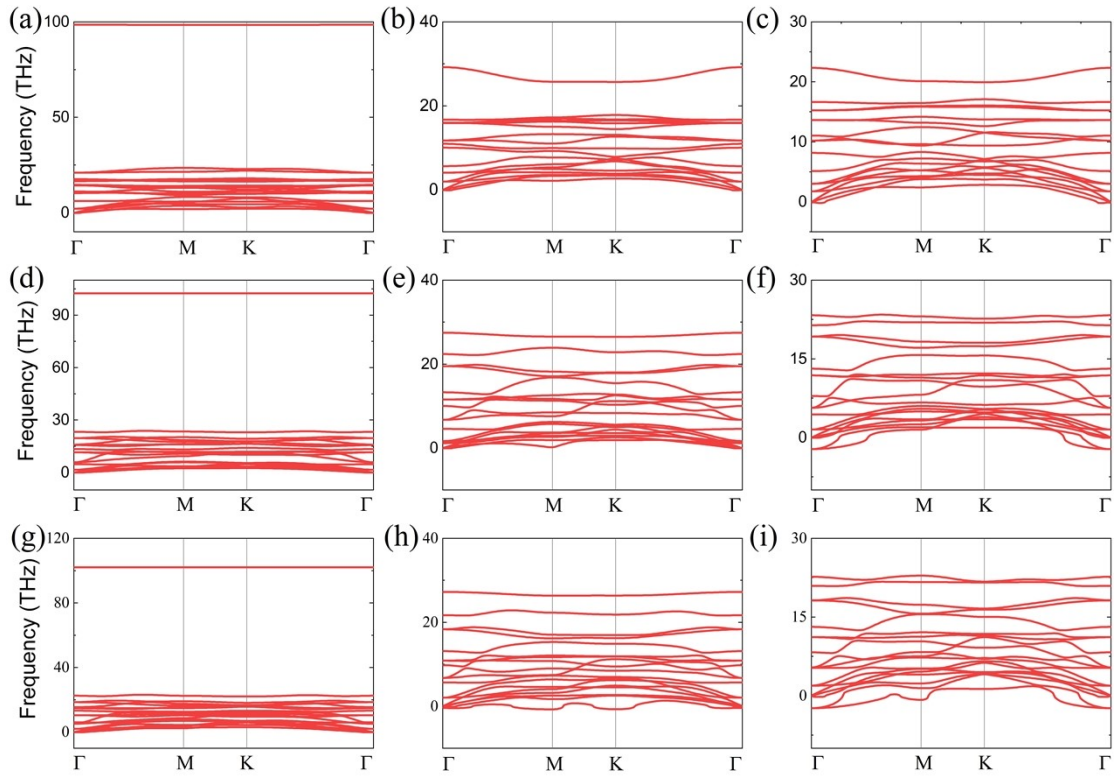


Fig. S14 Calculated phonon dispersion curves of 2D  $P3m1$   $M_2N_3X$  ( $M=\text{Cu}$ ,  $\text{Hf}$ , and  $\text{Zr}$ ;  $X=\text{H}$ ,  $\text{F}$  and  $\text{Cl}$ ) by the GGA-PBE functional: (a)  $\text{Cu}_2\text{N}_3\text{H}$ , (b)  $\text{Cu}_2\text{N}_3\text{F}$ , (c)  $\text{Cu}_2\text{N}_3\text{Cl}$ , (d)  $\text{Hf}_2\text{N}_3\text{H}$ , (e)  $\text{Hf}_2\text{N}_3\text{F}$ , (f)  $\text{Hf}_2\text{N}_3\text{Cl}$ , (g)  $\text{Zr}_2\text{N}_3\text{H}$ , (h)  $\text{Zr}_2\text{N}_3\text{F}$ , and (i)  $\text{Zr}_2\text{N}_3\text{Cl}$

In Fig. S14, the imaginary frequencies in 2D  $P3m1$  (f)  $\text{Hf}_2\text{N}_3\text{Cl}$ , (h)  $\text{Zr}_2\text{N}_3\text{F}$ , and (i)  $\text{Zr}_2\text{N}_3\text{Cl}$  indicate that these three phases are dynamically unstable.

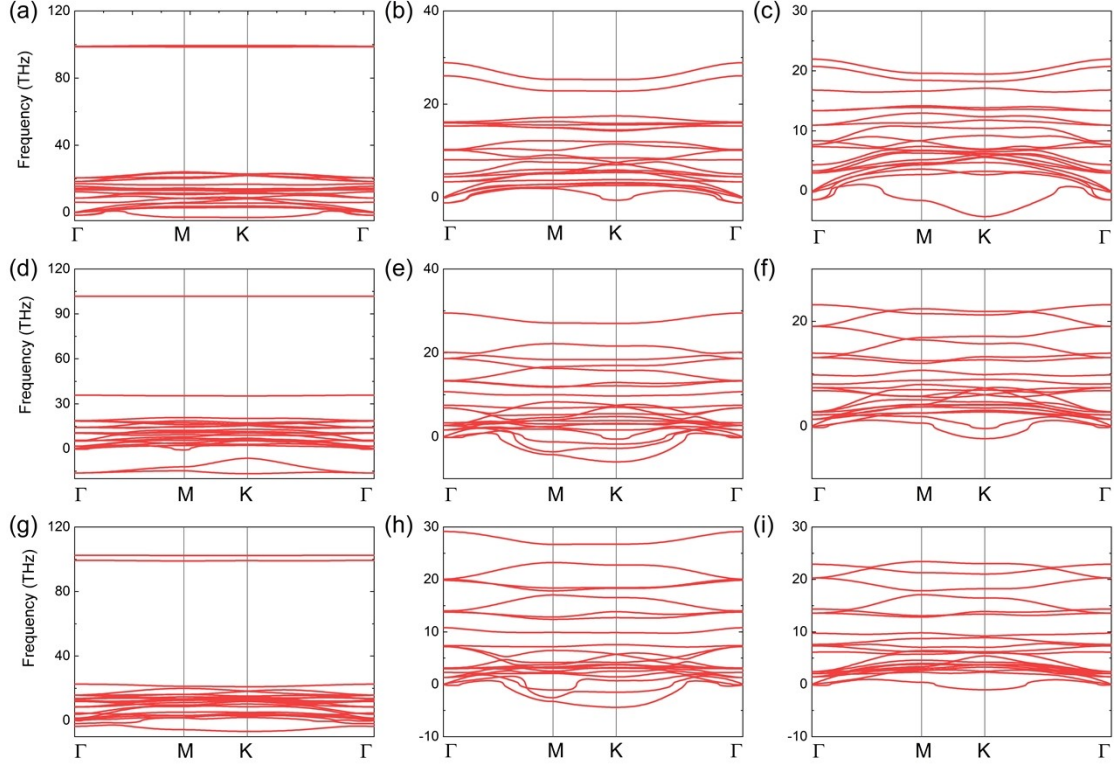


Fig. S15 Calculated phonon dispersion curves of 2D  $P3m1$   $M_2N_3X_2$  ( $M=\text{Cu, Zr, and Hf}$ ;  $X=\text{H, F, and Cl}$ ) by GGA-PBE functional: (a)  $\text{Cu}_2\text{N}_3\text{H}_2$ , (b)  $\text{Cu}_2\text{N}_3\text{F}_2$ , (c)  $\text{Cu}_2\text{N}_3\text{Cl}_2$ , (d)  $\text{Zr}_2\text{N}_3\text{H}_2$ , (e)  $\text{Zr}_2\text{N}_3\text{F}_2$ , (f)  $\text{Zr}_2\text{N}_3\text{Cl}_2$ , (g)  $\text{Hf}_2\text{N}_3\text{H}_2$ , (h)  $\text{Hf}_2\text{N}_3\text{F}_2$ , and (i)  $\text{Hf}_2\text{N}_3\text{Cl}_2$

In the Fig. S15, imaginary phonon modes are found for all 2D  $P3m1$   $M_2N_3X_2$  phases, confirming their dynamical instabilities.

Table S8 Calculated crystallographic parameters of 2D  $P3m1$   $\text{Cu}_2\text{N}_3\text{H}$ ,  $\text{Cu}_2\text{N}_3\text{F}$ ,  $\text{Cu}_2\text{N}_3\text{Cl}$ ,  $\text{Zr}_2\text{N}_3\text{H}$ ,  $\text{Hf}_2\text{N}_3\text{H}$ , and  $\text{Hf}_2\text{N}_3\text{F}$  by the GGA-PBE functional

Phase	Z	Space Group	Lattice parameters ( $\text{\AA},^\circ$ )	Atomic coordinates (fractional)
$\text{Cu}_2\text{N}_3\text{H}$	1	$P3m1$ SG 156	$a=b=3.10$ , $c=38.50$ , $\alpha=\beta=90.0, \gamma=120.0$	Cu 1c (0.67 0.33 0.83) Cu 1a (0.00 0.00 0.75) N 1a (0.00 0.00 0.80) N 1b (0.33 0.67 0.74) N 1b (0.33 0.67 0.85) H 1b (0.33 0.67 0.88)

$\text{Cu}_2\text{N}_3\text{F}$	1	<i>P3m1</i> SG 156	$a=b=3.12,$ $c=38.89,$ $\alpha=\beta=90.0, \gamma=120.0$	Cu 1c (0.67 0.33 0.83) Cu 1a (0.00 0.00 0.75) N 1a (0.00 0.00 0.80) N 1b (0.33 0.67 0.74) N 1b (0.33 0.67 0.85) F 1b (0.33 0.67 0.89)
$\text{Cu}_2\text{N}_3\text{Cl}$	1	<i>P3m1</i> SG 156	$a=b=3.15,$ $c=37.11,$ $\alpha=\beta=90.0, \gamma=120.0$	Cu 1c (0.67 0.33 0.83) Cu 1a (0.00 0.00 0.75) N 1a (0.00 0.00 0.80) N 1b (0.33 0.67 0.74) N 1b (0.33 0.67 0.85) Cl 1b (0.33 0.67 0.90)
$\text{Zr}_2\text{N}_3\text{H}$	1	<i>P3m1</i> SG 156	$a=b=3.43,$ $c=31.40,$ $\alpha=\beta=90.0, \gamma=120.0$	Zr 1c (0.67 0.33 0.84) Zr 1a (0.00 0.00 0.74) N 1a (0.00 0.00 0.80) N 1b (0.33 0.67 0.72) N 1b (0.33 0.67 0.87) H 1b (0.33 0.67 0.91)
$\text{Hf}_2\text{N}_3\text{H}$	1	<i>P3m1</i> SG 156	$a=b=3.39,$ $c=32.19,$ $\alpha=\beta=90.0, \gamma=120.0$	Hf 1c (0.67 0.33 0.83) Hf 1a (0.00 0.00 0.74) N 1a (0.00 0.00 0.80) N 1b (0.33 0.67 0.72) N 1b (0.33 0.67 0.87) H 1b (0.33 0.67 0.90)
$\text{Hf}_2\text{N}_3\text{F}$	1	<i>P3m1</i> SG 156	$a=b=3.41,$ $c=31.85,$ $\alpha=\beta=90.0, \gamma=120.0$	Hf 1c (0.67 0.33 0.83) Hf 1a (0.00 0.00 0.74) N 1a (0.00 0.00 0.80) N 1b (0.33 0.67 0.72) N 1b (0.33 0.67 0.87) F 1b (0.33 0.67 0.91)

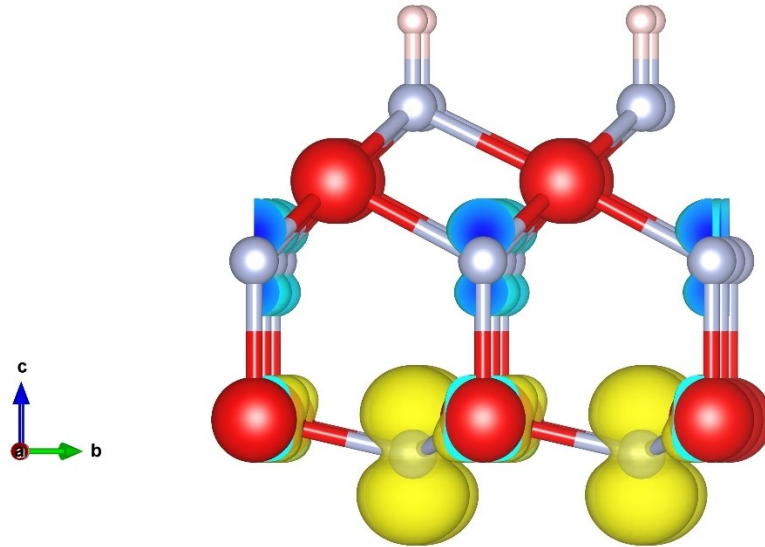


Fig. S16 Spin charge density of 2D  $P3m1$   $\text{Cu}_2\text{N}_3\text{X}$  ( $\text{X}=\text{H}, \text{F}$  and  $\text{Cl}$ ). The pink, silver and red balls are for X, N and Cu atoms, respectively.

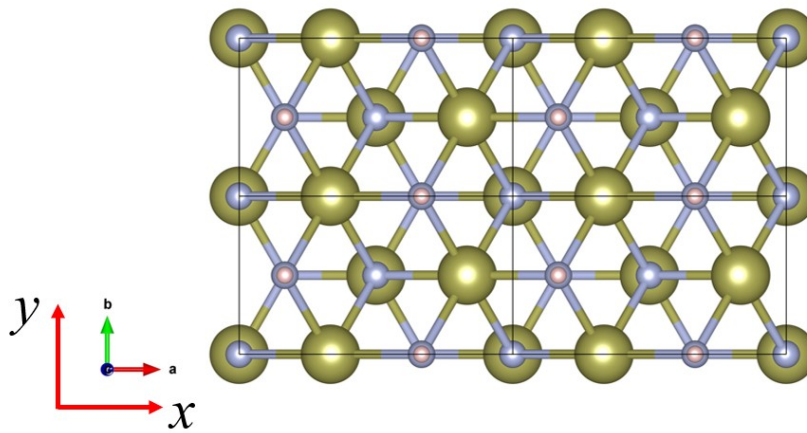


Fig. S17 Rectangular lattices of 2D  $P3m1$   $\text{Zr}_2\text{N}_3\text{H}$ ,  $\text{Hf}_2\text{N}_3\text{H}$ , and  $\text{Hf}_2\text{N}_3\text{F}$ . The silver, yellow and pink balls are for N, M (Zr, Hf), and X (H, F) atoms, respectively. The equivalent lattice parameters  $a$ ,  $b$  of this rectangular cell are defined as  $x_0$  and  $y_0$ , respectively.

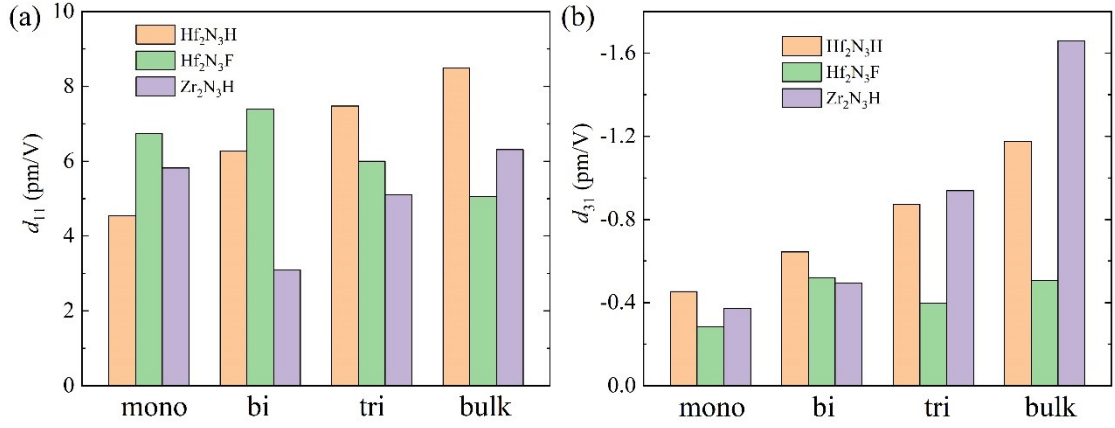


Fig. S18 Piezoelectric coefficients  $d_{11}$  (a, c) and  $d_{31}$  (b, d) of 2D  $P3m1$   $Zr_2N_3H$ ,  $Hf_2N_3H$ , and  $Hf_2N_3F$  via stacking effect. The mono, bi, and tri indicates the monolayer, trilayer, and trilayer of 2D  $P3m1$   $Zr_2N_3H$ ,  $Hf_2N_3H$ , and  $Hf_2N_3F$ , respectively.

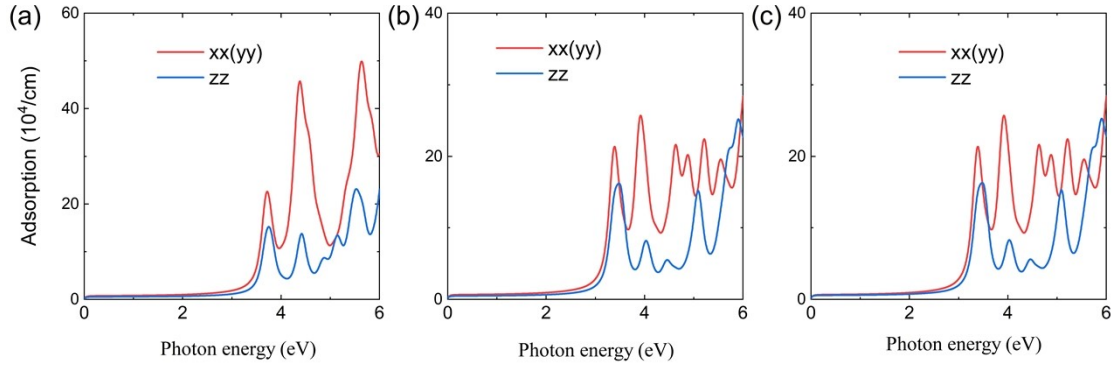


Fig. S19 The calculated optical absorptions of (a) 2D  $P3m1$   $Zr_2N_3H$ , (b) 2D  $P3m1$   $Hf_2N_3H$ , (c) 2D  $P3m1$   $Hf_2N_3F$  along different spatial directions

### S3. Reference

1. G. Kresse and J. Furthmüller, *Phys. Rev. B*, 1996, **54**, 11169.
2. G. Kresse and J. Furthmüller, *Comput. Mater. Sci.* 1996, **6**, 15-50.
3. P. E. Blöchl, *Phys. Rev. B*, 1994, **50**, 17953.
4. J. P. Perdew, K. Burke and M. Ernzerhof, *Phys. Rev. Lett.*, 1998, **80**, 891.
5. J. Heyd, G. E. Scuseria and M. Ernzerhof, *J. Chem. Phys.*, 2003, **118**, 8207-8215.
6. T. A. Manz and N. G. Limas, *RSC Adv.*, 2016, **6**, 47771-47801.
7. W. Tang, E. Sanville and G. Henkelman, *J. Phys. Condens. Matter*, 2009, **21**, 084204.
8. K. Momma and F. Izumi, *J. Appl. Crystallogr.*, 2011, **44**, 1272-1276.
9. A. Togo, F. Oba and I. Tanaka, *Phys. Rev. B*, 2008, **78**, 134106.
10. M. Born, K. Huang and M. Lax, *Am. J. Phys.*, 1955, **23**, 474-474.
11. R. Cowley, *Phys. Rev. B*, 1976, **13**, 4877.
12. F. Mouhat and F.-X. Coudert, *Phys. Rev. B*, 2014, **90**, 224104.
13. Y. Le Page and P. Saxe, *Phys. Rev. B*, 2002, **65**, 104104.
14. C. Jasiukiewicz, T. Paszkiewicz and S. Wolski, *Phys. Status. Solidi. (b)*, 2008, **245**, 557-561.
15. L. Wang, A. Kutana, X. Zou and B. I. Yakobson, *Nanoscale*, 2015, **7**, 9746-9751.
16. H. Zhang, J. Wang, F. Guégan and G. Frapper, *Nanoscale*, 2023, **15**, 7472-7481.
17. Andersen, H. C. *J. Chem. Phys.*, 1980, **72**, 2384-2393.
18. Y. Xu, H. Zhang, H. Shao, G. Ni, J. Li, H. Lu, R. Zhang, B. Peng, Y. Zhu and H. Zhu, *Phys. Rev. B*, 2017, **96**, 245421.
19. Y. Cai, G. Zhang and Y.-W. Zhang, *J. Am. Chem. Soc.*, 2014, **136**, 6269-6275.
20. S.-D. Guo, W.-Q. Mu and Y.-T. Zhu, *J. Phys. Chem. Solids*, 2021, **151**, 109896.
21. S. Baroni, S. De Gironcoli, A. Dal Corso and P. Giannozzi, *Rev. Mod. Phys.*, 2001, **73**, 515.
22. M. N. Blonsky, H. L. Zhuang, A. K. Singh and R. G. Hennig, *ACS Nano*, 2015, **9**, 9885-9891.
23. K. Wang, W. Zhou, Y. Cheng, M. Zhang, H. Wang and G. Zhang, *Nanoscale*, 2021, **13**, 10882-10890.
24. D. Li, J. Gao, P. Cheng, J. He, Y. Yin, Y. Hu, L. Chen, Y. Cheng and J. Zhao, *Adv. Funct. Mater.*, 2020, **30**, 1904349.
25. K. Gaál-Nagy, *Phys. Rev. B*, 2008, **77**, 024309.